METALLURGY

How hair deforms steel

Gianluca Roscioli[1], Seyedeh Mohadeseh Taheri-Mousavi[1,2], Cemal Cem Tasan[1]*

Steels for sharp edges or tools typically have martensitic microstructures, high carbide contents, and various coatings to exhibit high hardness and wear resistance. Yet they become practically unusable upon cutting much softer materials such as human hair, cheese, or potatoes. Despite this being an everyday observation, the underlying physical micromechanisms are poorly understood because of the structural complexity of the interacting materials and the complex boundary conditions of their co-deformation. To unravel this complexity, we carried out interrupted tests and in situ electron microscopy cutting experiments with two micromechanical testing setups. We investigated the findings analytically and numerically, revealing that the spatial variation of lath martensite structure plays the key role leading to a mixed-mode II-III cracking phenomenon before appreciable wear.

Humankind has optimized materials and processes to produce sharp edges for millennia, to be used as utensils (*1*), swords (*2*), blades (*3*), and other tools. Cutting processes today are routinely used in various industries, including medicine (*4*), manufacturing (*5*), food processing (*6*), and home appliances (*7*). Although each application creates specific engineering requirements, the overall material design aim is typically the same: achieving high sharpness and hardness. A typical metallic material used for blades in straight razors, for example, is a carbide-rich lath martensitic stainless steel, honed to a wedge geometry (*8*) with an angle of 17° and a tip radius of 40 nm to obtain the desired sharpness (*9*) (Fig. 1A). This material is coated with even harder materials (*10*) such as diamond-like carbon (*7*) and a final polytetrafluoroethylene layer to reduce friction (*11*, *12*). Even then, as commonly experienced by razor blade users, the hard lath martensitic steel progressively loses its functionality upon cutting hair, a material that is softer by more than one order of magnitude (hardness scale in Fig. 1A). Such material performance degradations are common in other cutting operations as well (*5*, *13*, *14*), creating operational and environmental consequences (*15*). Kitchen knives, for example, get dull (*16*, *17*) upon cutting soft materials such as cheese (*18*) or potatoes (*19*). As commonly practiced, resharpening resets the cutting capabilities of dull knives (*20*, *21*), creating the general conception that wear mechanisms are responsible for the performance degradation of sharp metallic edges, including martensitic steel razor blades (*22*).

Although wear does occur during haircutting (*5*, *23*, *24*), the failure mechanisms are more complex for two reasons. First, the two interacting materials have hierarchical microstructures with anisotropic and size-dependent mechanical responses (*25*, *26*) (Fig. 1A). Lath martensitic steels have a hierarchy (*27*) of prior-austenite, packet, block, subblock, and lath boundaries (*28*–*30*) (Fig. 1A) and a high density of heterogeneously distributed dislocations (*31*, *32*). Interstitial carbon is trapped in solid solution during quenching, but tempering or autotempering can lead carbon to decorate dislocations (*25*, *33*) or precipitate as carbides (*34*). All these structural features provide ferrous martensite with high hardness but a nonuniform micromechanical response (*35*–*37*). Similarly, human hair is a highly anisotropic composite with a noncircular cross section and an average diameter ranging between 80 and 200 μm. The outer layer is the ~170-MPa hard cuticle (*38*) that forms a shell with cells arranged like shingles on a roof (Fig. 1A). The middle layer, the cortex, is three times softer and composed of a hierarchy of fibrils elongated along the hair direction. The medulla is the hollow inner layer and has little mechanical contribution to the cutting response (*39*). Because hair is hygroscopic, in the presence of moisture its cell structure is altered to accommodate water molecules, lowering both elastic modulus and yield strength (*26*, *39*). Both the blade and the hair are anisotropic and exhibit size-dependent mechanical behavior. This generates a mechanical response that depends on the stress state and on the volume that contributes to deformation.

Second, the boundary conditions of their co-deformation can vary dynamically, even during a single cutting operation (Fig. 1B). During shaving, each single hair can be represented as a flexible cantilever, quasi-fixed at the end toward the skin and completely free at the other. In this configuration, the hair is free to bend when the blade approaches it and penetrates in it during the cut, influencing the mode of deformation (Fig. 1B). The hair is predominantly experiencing mode I opening. Depending on whether the hair is bending or not (Fig. 1B), the stress is applied (i) on both surfaces of the crack (straight indentation, $\gamma = 0°$) or (ii) only on one of the two surfaces. This results in a pure mode II stress on the blade in the former case or a mixed-mode II-III stress in the latter one. The geometry of the cutting problem further necessitates that, at different stages of cutting, different volumes of the two materials interact and contribute to the deformation process.

These complexities call for systematic experiments to investigate the interaction of the two materials. To this end, we investigated martensitic stainless steel blades (Fig. 1A) typical of commercial safety razors (fig. S1). Scanning electron microscope (SEM) and electron backscatter diffraction (EBSD) analyses revealed their lath martensitic matrix (Fig. 1A) with heterogeneously distributed carbides (Fig. 1A, inset). The honing process causes deformation of the microstructure within ~5 μm of the tip (*8*), as highlighted in the EBSD image quality (fig. S2F), kernel average misorientation (fig. S2D), and grain boundary maps (fig. S2E). We measured hardness values within 70 μm from the tip using an in situ SEM picoindenter and conducted nanoindentation experiments in the bulk material, revealing an average hardness value of 8.7 ± 0.7 (SD) GPa. This statistical variation can arise because of the presence of carbides, retained austenite, and martensite substructure heterogeneity (*25*, *27*–*32*, *40*). Edge effects prevented confirmation of a hardness increase near the tip implied by the deformed zone.

To measure blade wear evolution in real shaving conditions, we performed interrupted tests on disposable razor cartridges (sample 1 in fig. S1) by tracking different regions using SEM analyses after different stages of use (fig. S3 and movie S1). We quantified the average blade wear rate along the sharp edge using image analysis, although contamination-induced charging limits the accuracy of this method (fig. S3E). The level of wear was low: 12 nm^3/nm after 5 shaves and 13 nm^3/nm after 10 shaves. However, these interrupted tests revealed the occurrence of chips along the sharp edge (Fig. 1C). Although sharp at the macroscale, the edges of razor blades are asperous at the microscale, even in the unused condition (Fig. 1C-1). We observed that microcrack nucleation takes place from these asperities during haircutting (Fig. 1C-2). Only a small fraction of the asperities proceed to form microcracks, and these are not necessarily the largest asperities present along the edge. These microcracks initially propagate orthogonally to the edge (Fig. 1C-2) before deviating their direction to form the final chip geometry (Fig. 1C-3). The deformation marks (Fig. 1C-2) show that the portion of the sharp edge that belongs to the chip being

[1]Department of Materials Science and Engineering, Massachusetts Institute of Technology, 77 Massachusetts Avenue, Cambridge, MA 02139, USA. [2]Department of Mechanical Engineering, Massachusetts Institute of Technology, 77 Massachusetts Avenue, Cambridge, MA 02139, USA.
*Corresponding author. Email: tasan@mit.edu

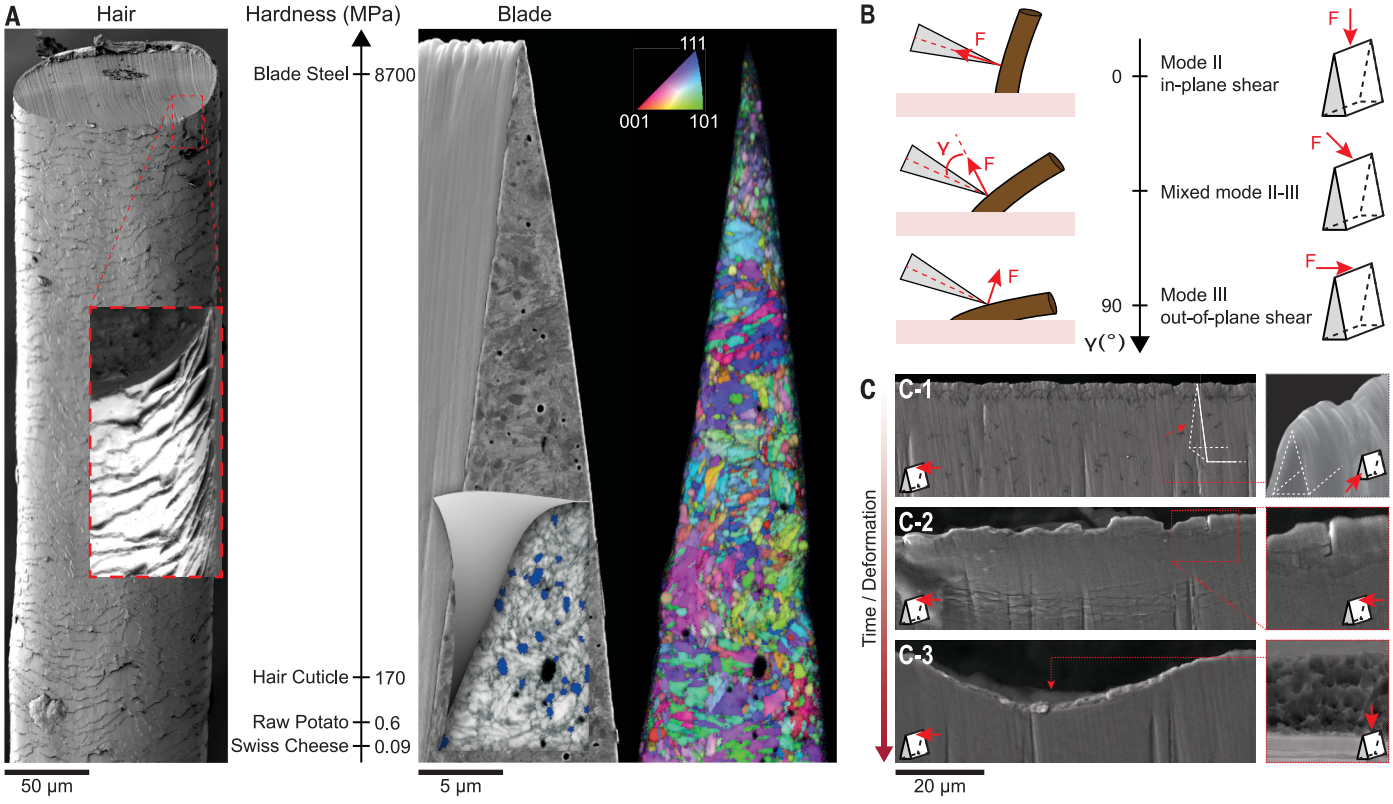

Fig. 1. Materials and mechanics of the shaving process. (**A**) Human hair and martensitic steel blades both have complex hierarchical structures. The former is a layered anisotropic material; meanwhile, the latter has a fine lath martensitic matrix structure (EBSD–Inverse Pole Figure map) with heterogeneously distributed carbides (highlighted in blue in the inset). As shown by the scale, the difference in the hardness of these two materials is substantial (~50 times). (**B**) Stress state on the blade during haircutting depends on the force angle γ, so that any configuration between pure in-plane and out-of-plane shear is possible. (**C**) Deformation sequence of a blade from unused conditions (C-1) to initial crack nucleation at the sharp edge and localized bending (C-2) to final ductile failure (C-3).

created rigidly bends out of plane as the microcrack changes direction. The presence of dimples on the resulting fracture surface reveals that the martensitic structure exhibits ductile deformation before fracture (Fig. 1C-3). The hard coatings, by contrast, exhibited brittle fracture features resulting from the bending of the substrate (fig. S4).

To better understand the development of this failure process before the activation of other failure modes (fatigue, corrosion, and wear), we carried out 25 in situ SEM tests using a microdeformation stage with customized clamps that can hold a blade on one side and single or multiple hair(s) on the other [Fig. 2, fig. S5, and movies S2 to S4, (*38*)]. Running in situ SEM tests enables expedited investigation of the underlying damage mechanisms, because the dry cutting conditions in the SEM should increase the haircutting force. Even then, we did not observe blade deformation or chipping for straight orthogonal cuts, in which there is no out-of-plane force component. By contrast, creating a more realistic condition by tilting the blade 21° to the cutting direction (Fig. 2B) led to an out-of-plane force component and, in turn, to plastic deformation and chipping in several cases (Fig. 2C and movie S2). Tests using hairs of different diameters allowed us to conclude that the size of the chips is not dominated by the diameter of the hair or the number of hairs sequentially cut, nor by the cutting angle alone. The same portion of a sharp edge can cut several hairs with different cutting angles γ (Fig. 1B), leading to no visible deformation, until the blade suddenly fails (fig. S6 and movie S3). We also discovered that the chips most commonly appear in correspondence to the edges of the hair. For example, one single hair can produce two chips in the blade, each of them starting from one edge of the hair (Fig. 2C). In addition, we observed that the chips generally extended beyond the ~5-μm highly deformed region near the tip of the blade (Fig. 1C), suggesting that the observed phenomenon is not dominated by honing-induced effects. Last, the comparison of the SEM images from the dry in situ experiments (Fig. 2C) and from the wet interrupted tests (Fig. 1C) reveals identical failure mechanism in both cases (except the increased failure rate in the former), confirming the validity of the expedited in situ approach.

We used three-dimensional parametric finite element simulations to identify the role of asperities and the direction of the applied load on deformation and chipping (Fig. 3, A to C). We modeled the martensitic steel as a homogeneous isotropic elasto-plastic material with a yield strength of ~1690 MPa and flow behavior as determined by our tensile tests (fig. S7). We added notches with a size determined by our SEM analyses (e.g., Fig. 1C-1) to replicate an extreme condition of the asperities along the sharp edge and simulated the cutting stress on the blade as an evenly distributed surface traction acting only on one side [Fig. 3A, (*38*)], with a magnitude of 50 MPa. To determine this value, we measured the force to cut a single hair by carrying out dedicated in situ SEM single-hair cutting-force measurements using a picoindenter, with tip and sample holder modified to host the blade on one side and a single hair on the other (Fig. 2, D to F). Representative results are shown in Fig. 2F and in movie S4, revealing a maximum value of ~0.2 N independent of hair diameter or cross-sectional shape (fig. S8).

Our first simulations focused on identifying the location of the highest stress intensity

notch, as a function of the direction of the applied stress. As seen in Fig. 3B, a straight indentation of the hair (surface traction of 0°) produces stress intensification at the notches in contact with the hair, but the values are not high enough to promote plastic deformation. Cutting the hair at an angle, instead, produces higher stress values in the region of the blade contacted by the hair, with a maximum stress at the notch in contact with the edge of the hair. Our analysis of the von Mises stresses as a function of the surface traction angle (Fig. 3C) showed that (i) the stress at the tip of the notches does not change substantially if the surface traction direction is contained in the blade cross section (for cutting angles below 8.5°); (ii) the stress at the tip of the notches in contact with the hair increases with the cutting angle for angles above this value; (iii) meanwhile, it decreases for notches not in contact with the hair; and (iv) the highest stress intensification occurs at the notch in contact with the edge of the hair. Our simulation results are consistent with the in situ SEM haircutting experiments (Fig. 2C), in which the chips preferentially nucleated at positions in contact with the edge of the hair.

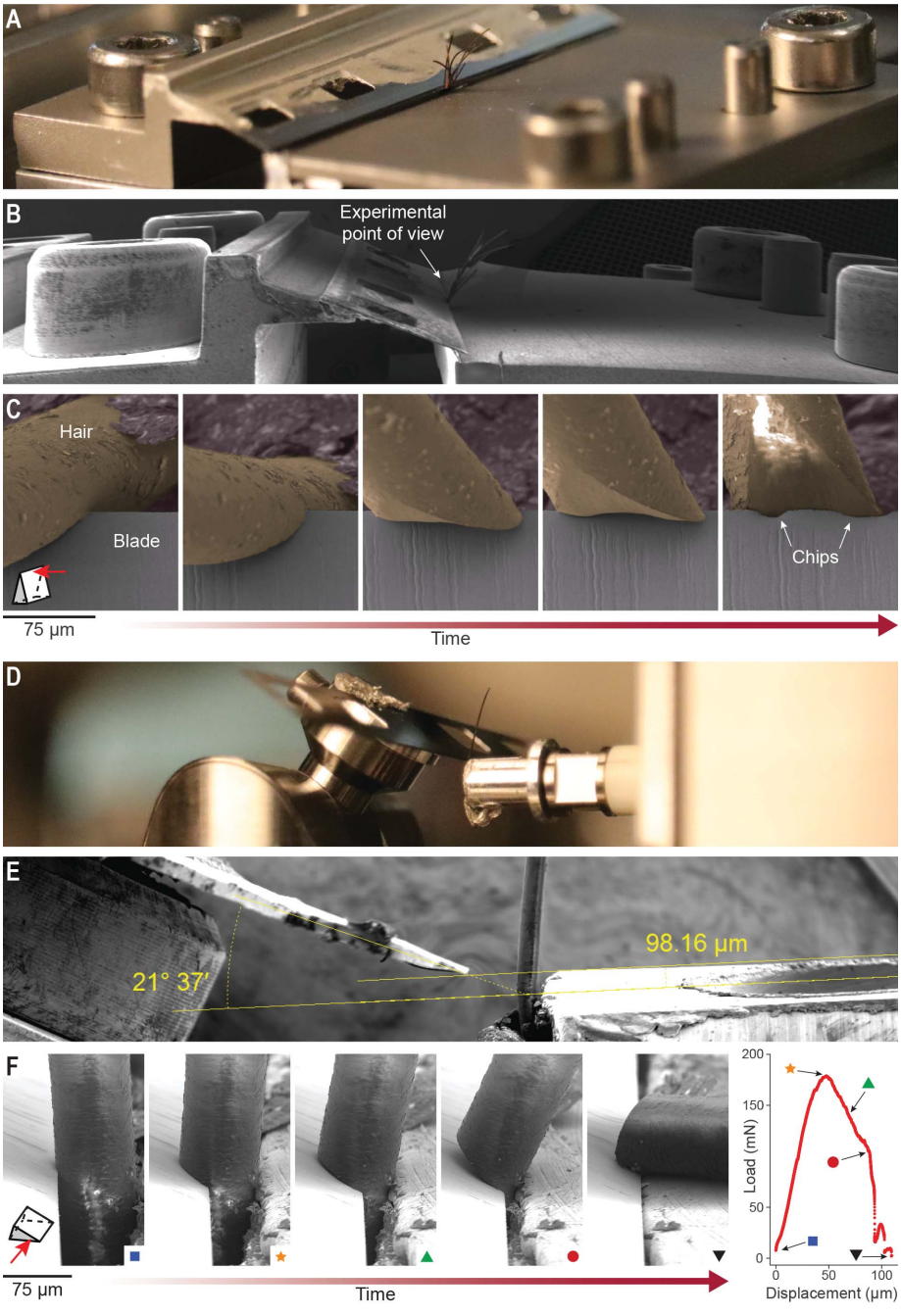

Fig. 2. Two sets of in situ SEM haircutting experiments. (**A** to **C**) Multihair cutting experiments to identify the underlying damage mechanisms. (A) and (B) show optical and SEM images of the experimental setup used to cut multiple hairs in situ; meanwhile, (C) provides a representative example of the results through a sequence of images (colored from movie S2) in which a single hair produces two chips in the blade. The waviness of the honing marks on the blade is an imaging artifact due to the blade advancing in a vertical direction during imaging. (**D** to **F**) Single-hair in situ SEM cutting-force measurements. (D) and (E) show optical and SEM images of the experimental setup; meanwhile, (E) provides a representative result through a sequence of experimental images corresponding to points highlighted in the load-displacement plot.

We observed microcracking and chipping at lower angles than those suggested in the simulations (fig. S6 and movie S3). To explain this, we hypothesized a process that links the heterogeneity of the lath martensitic structure to an increase in microcracking sensitivity (Fig. 3, D to H). We adapted an analytical model to calculate the energy release rate of an interfacial lateral crack in a thin, bimaterial, semi-infinite plate with constant thickness to our mixed-mode II-III problem, with the crack potentially propagating along the interface between the two materials [Fig. 3D, (*38*)]. We applied a 50-MPa stress while varying the direction of the load between pure mode II and pure mode III and considered materials with identical Poisson's ratio (0.3) but different Young's moduli. The small modulus variations we introduced follow the values we obtained from the continuous-stiffness-measurement mode nanoindentation experiments on the lath martensitic steel (fig. S9). The energy release rate increases when moving from pure mode II to pure mode III (Fig. 3D). Changing the Young's moduli of the two materials while keeping their average constant produces an upward shift of the energy release rate curve: A larger difference between the two moduli creates a greater shift (Fig. 3D). This corresponds to a higher probability of crack propagation for two dissimilar materials than for a homogeneous one with a similar average property.

We conducted another set of three-dimensional parametric simulations to analyze the energy release rate at the tip of a single notch in a blade, considering its wedge geometry with increasing thickness ahead of the notch and different crack propagation directions [Fig. 3, E to H; (*38*)]. We used a single or two different materials on the opposite sides of the notch. The energy release rate for a crack propagating along the original crack direction (θ = 0°) increases as the mode III component of the stress increases (Fig. 3F). The energy release rate also varies with the crack propagation direction (Fig. 3G). The critical direction, corresponding to the maximum energy release rate, depends on both loading direction and material combination (Fig. 3H). When the load is applied on a compliant

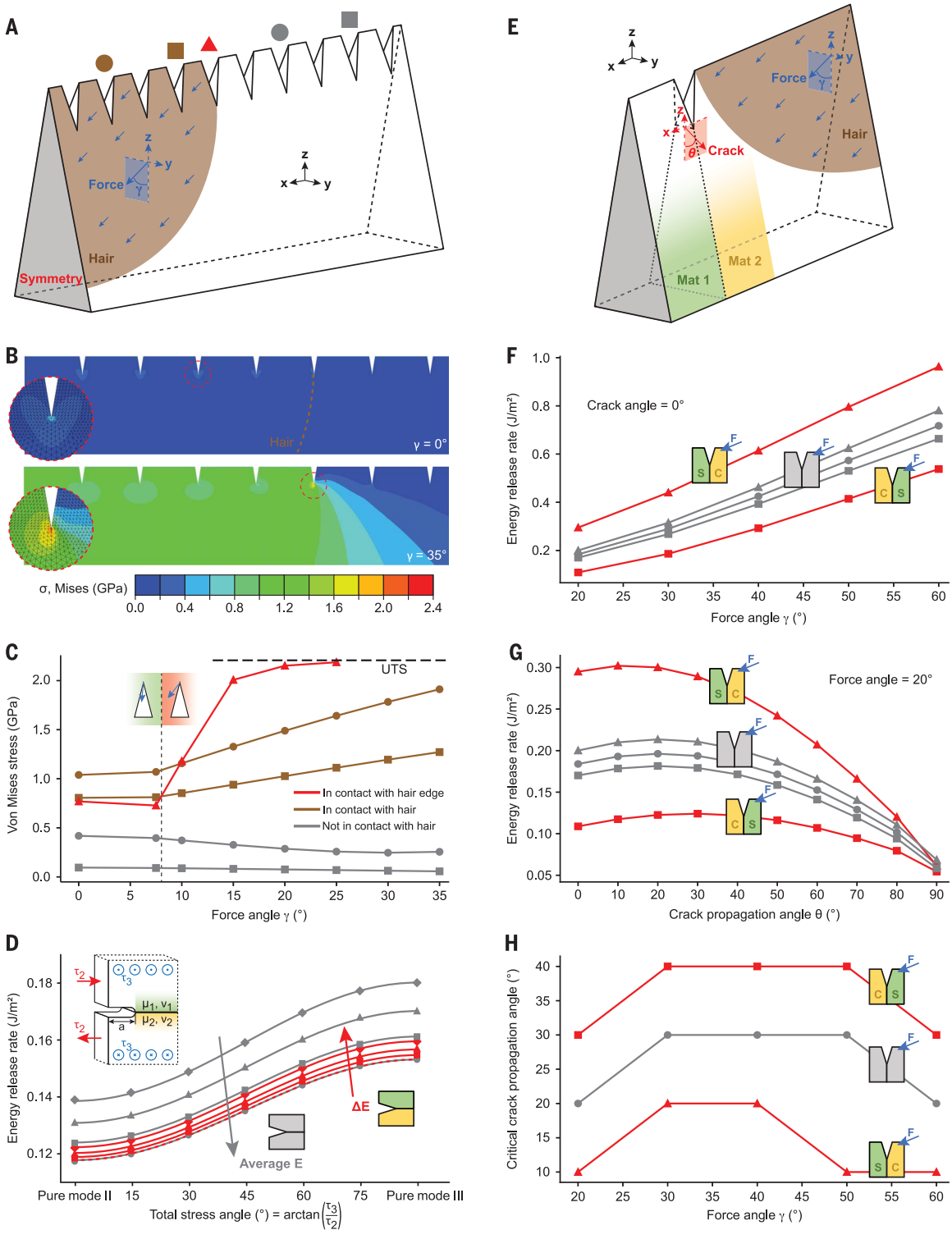

Fig. 3. Notch with critical stress intensification during haircutting, and energy release rate dependence on material heterogeneity and force angle. (**A**) Simulation model to identify the position of the notch with critical stress intensification as a function of the angle of the force imparted by the hair. The first four notches from the left are in contact with the hair, the fifth notch is in contact with the hair edge [brown dashed line in (B)], and the other notches are not in contact with the hair. (**B**) Von Mises stress distribution along the midplane of the blade resulting from a straight indentation (top) and a force oriented at 35° (bottom). (**C**) Plots of the von Mises stress evolution at the tip of selected notches as a function of the force angle γ, using the color code and marker shapes reported in (A). UTS, ultimate tensile strength. (**D**) Results of the analytical model (model in the inset) for a thin, bimaterial, semi-infinite plate with constant thickness and a lateral notch at the interface. E, Young's modulus. (**E** to **H**) Model (E) and results (F to H) of finite element simulations to determine energy release rate dependence on material (Mat) heterogeneity and force angle γ for a crack propagating from the notch with critical stress intensification (near the edge of the hair) along different possible crack propagation angles θ. In (D) and (F to H), gray and red curves represent homogeneous and heterogeneous materials, respectively. C, compliant (modulus of 170 GPa); F, force; S, stiff (modulus of 200 GPa).

material next to a stiff one (C and S in the schematic, respectively) with an interfacial notch, the crack is more likely to propagate than in the reversed configuration. The critical crack propagation angle in this situation is also smaller (Fig. 3G). Furthermore, the microcracks nucleated at the sharp edge propagate at an angle with respect to the blade axis (*z* axis in Fig. 3E), deviating toward the region of application of the load. This propagation path is determined both by the asymmetric mode II component of the force, which promotes crack kinking out of its original plane (*41*, *42*), and by the geometry of the blade, with a thickness increasing along

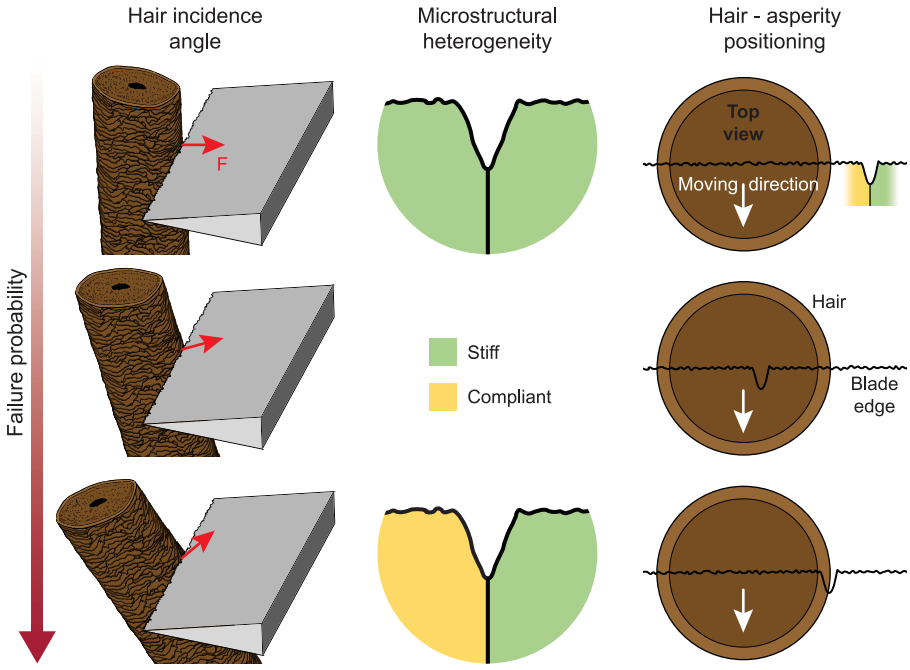

Fig. 4. Critical factors for lath martensite failure upon cutting hair. The three factors affecting razor blade chipping are shown from left to right: (i) hair incidence angle, (ii) heterogeneity present in the microstructure and at the asperities along the sharp edge, and (iii) relative position between an asperity and the edge of the hair when it is halfway through the cut. Failure probability depends on whether these conditions are simultaneously met.

the blade axis. Assuming that the surface energy of the material is constant, the energy penalty for the crack to stay along this axis is higher than it would be to propagate in a direction of constant (or less increasing) thickness, as staying along this axis would produce a larger surface per unit length of propagation. For the same reason, the crack will ultimately turn backward toward the sharp edge, forming a chip.

To confirm the mechanistic effects of microstructural heterogeneity predicted by our analytical and numerical results, we conducted in situ SEM haircutting experiments with focused ion beam half-milled blades, which enable visualization of the microstructure during deformation (fig. S10). The milling creates contrast between the martensitic matrix and the carbides, allowing us to unravel damage mechanisms. In this experiment, we observed that the microcracks typically nucleated (i) at martensite-carbide boundaries that neighbor an asperity (fig. S10B, left) and (ii) when the hair was in contact with the more compliant constituent. The microcracks then propagated at an angle, causing decohesion at multiple carbide-matrix boundaries or carbide cracking (fig. S10B, right), as well as microplasticity in martensitic regions in between.

With our experimental, analytical, and numerical results, we have shown that haircutting can induce damage nucleation, growth, and coalescence (in the form of chipping) in lath martensitic steel and that these occur before other proposed failure modes due to wear effects (*5*, *14*, *16*, *17*, *43*, *44*) or brittleness of the hard coatings (*5*, *24*, *43*, *45*). This failure process requires the concurrence of (i) sufficient levels of hair bending to create stresses with a considerable mode III component; (ii) processing-induced asperities on the blade edge with microstructural constituents of sufficiently different properties on either side; and (iii) positioning of the hair such that the outermost circumferential point is aligned with such an asperity (to produce the highest stress intensification) and in contact with the side containing the more compliant constituent (Fig. 4). Because these conditions are simultaneously met only in rare cases, hair-induced chipping is not common, and typical commercial blades fail only after multiple uses. The presence of multiple criteria also demonstrates why stand-alone postmortem or in situ analyses cannot reveal the full nature of this complex fracture process.

Current design philosophy for cutting tool materials follows the Archard law, which linearly correlates the average hardness of an annealed metal to its wear resistance. The failure recipe identified above suggests [along with wedge angle increase, which would be at the expense of the sharpness (*9*, *46*)] reconsideration of the microstructure design guidelines toward the reduction of asperities and microcracking tendencies, both of which arise as a result of structural heterogeneity. In case of fine lath martensite, several microstructural constituents of contrasting mechanical behavior can be larger than the blade tip radius (~40 nm) (Fig. 1A) (*25*, *27*–*32*, *35*). This creates spatial variation of mechanical properties along the sharp edge, with different constituents at different positions. This heterogeneity can be beneficial because a microcrack is less likely to propagate in a heterogeneous structure than in a homogeneous one as long as the hair being cut gets in contact with a stiff constituent neighboring a compliant constituent (Fig. 3F). However, this ideal scenario is impossible to guarantee during the haircutting process, and the opposite scenario favoring microcrack propagation is equally likely. Consequently, additional microcracks will form from carbide cracking or carbide-matrix decohesion, further opening as microvoids (*47*, *48*), coalescing, and eventually resulting in ductile failure (Fig. 1C-3). The heterogeneity in the blade also lowers the minimum force angle for a crack to propagate in the material. Given a critical value for the energy release rate, independent of the loading direction (*41*), a heterogeneous configuration at an asperity reaches this critical value for smaller force angles than a homogeneous one (Fig. 3F). The chip shape and size variations we observed are also linked to the heterogeneity of the material being cut (Fig. 3H). Both depend on the initial critical crack propagation angle for which the energy release rate is maximum. A large critical angle will lead to short, shallow chips, whereas a small critical angle will lead to longer and deeper chips. Asperity formation during processing is also linked to microstructure heterogeneity. For example, for the lath martensitic steel we tested, honing causes strain localization and carbide knockoff, resulting in a rough edge at the microscale. All of these insights suggest the design of hard but more homogeneous microstructures for cutting tools. This can be realized by creating even finer structures at sharp edges, for instance, by further refining martensitic structure, by creating other nanostructured alloys to benefit from size effects, or even by avoiding crystallinity altogether (*49*–*51*). The ability to produce more efficient and longer-lasting sharp edges would also have a favorable environmental impact by lengthening material lifetime, motivating further investigations.

REFERENCES AND NOTES

1. E. H. Cline, *The Oxford Handbook of the Bronze Age Aegean* (Oxford Univ. Press, 2012); www.oxfordhandbooks.com/view/10.1093/oxfordhb/9780199873609.001.0001/oxfordhb-9780199873609.
2. D. Sapiro, B. Webler, *JOM* **68**, 3180–3185 (2016).
3. J. D. Verhoeven, *Sci. Am.* **284**, 74–79 (2001).
4. D. Black, R. Marks, A. Caunt, *Bioeng. Skin* **1**, 111–123 (1985).

5. D. Petersen, R. Link, K. Budinski, *J. Test. Eval.* **25**, 226 (1997).
6. R. W. McGorry, P. C. Dowd, P. G. Dempsey, *Appl. Ergon.* **36**, 71–77 (2005).
7. G. E. Gregory, R. C. Hamby, *Surf. Eng.* **16**, 373–378 (2000).
8. W. I. Nissen, R. M. Atwater, Methods and apparatus for sharpening razor blades or similar cutting tools, U.S. Patent 3,461,616A (1966); https://patents.google.com/patent/US3461616.
9. C. T. McCarthy, M. Hussey, M. D. Gilchrist, *Eng. Fract. Mech.* **74**, 2205–2224 (2007).
10. R. L. Moore, *Thin Solid Films* **270**, 331–334 (1995).
11. C. J. Clipstone, S. Hahn, N. Sonnenberg, C. White, A. Zhuk, Razor blade technology, U.S. Patent 6,684,513B1 (2004); https://patents.google.com/patent/US6684513.
12. O. H. Claus *et al*., Razor blades, U.S. 9,079,321B2 (2015).
13. C. Arcona, T. A. Dow, *J. Mater. Sci.* **31**, 1327–1334 (1996).
14. G. Keturakis, V. Lisauskas, *Mater. Sci. Medzg.* **16**, 205–209 (2010).
15. U.S. Environmental Protection Agency (EPA), "Environmental Consumer's Handbook" (EPA, 1990); https://nepis.epa.gov/Exe/ZyPDF.cgi/2000URC7.PDF?Dockey=2000URC7.PDF.
16. J. Marsot, L. Claudon, M. Jacqmin, *Appl. Ergon.* **38**, 83–89 (2007).
17. S. Schuldt, G. Arnold, J. Kowalewski, Y. Schneider, H. Rohm, *J. Food Eng.* **188**, 13–20 (2016).
18. N. Vásquez *et al*., *J. Food Eng.* **219**, 8–15 (2018).
19. N. Özkan, H. Xin, X. D. Chen, *J. Food Sci.* **67**, 1814–1820 (2002).
20. O. Hallén, *Nature* **173**, 958 (1954).
21. J. Karltun, K. Vogel, M. Bergstrand, J. Eklund, *Appl. Ergon.* **56**, 92–100 (2016).
22. Q. Zhu, J. Li, J. Zhang, C. Shi, *J. Mater. Eng. Perform.* **28**, 4511–4521 (2019).
23. T. Tamaoki, A. Okada, K. Uemura, Y. Uno, *J. Japan Soc. Precis. Eng.* **79**, 950–954 (2013).
24. M. I. Mendelson, in *Ceramic Engineering and Science Proceedings*, vol. 22 (Loyola Marymount University, 2001), pp. 293–300.
25. L. Morsdorf, C. C. Tasan, D. Ponge, D. Raabe, *Acta Mater.* **95**, 366–377 (2015).
26. S. M. Thozhur, A. D. Crocombe, P. A. Smith, K. Cowley, N. Mullier, *J. Mater. Sci.* **41**, 1109–1121 (2006).
27. L. Qi, A. G. Khachaturyan, J. W. Morris Jr., *Acta Mater.* **76**, 23–39 (2014).
28. C. C. Kinney, K. R. Pytlewski, A. G. Khachaturyan, J. W. Morris Jr., *Acta Mater.* **69**, 372–385 (2014).
29. S. Morito, H. Saito, T. Ogawa, T. Furuhara, T. Maki, *ISIJ Int.* **45**, 91–94 (2005).
30. S. Morito, H. Tanaka, R. Konishi, T. Furuhara, T. Maki, *Acta Mater.* **51**, 1789–1799 (2003).
31. S. Morito, X. Huang, T. Furuhara, T. Maki, N. Hansen, *Acta Mater.* **54**, 5323–5331 (2006).
32. T. Ohmura, A. M. Minor, E. A. Stach, J. W. Morris, *J. Mater. Res.* **19**, 3626–3632 (2004).
33. C. Lerchbacher, S. Zinner, H. Leitner, *Micron* **43**, 818–826 (2012).
34. J. Zhang, L. Morsdorf, C. C. Tasan, *Mater. Charact.* **111**, 137–146 (2016).
35. L. Morsdorf *et al*., *Acta Mater.* **121**, 202–214 (2016).
36. A. Shibata, T. Nagoshi, M. Sone, S. Morito, Y. Higo, *Mater. Sci. Eng. A* **527**, 7538–7544 (2010).
37. T. Ohmura, K. Tsuzaki, S. Matsuoka, *Scr. Mater.* **45**, 889–894 (2001).
38. Materials and methods are available as supplementary materials.
39. B. Bhushan, C. LaTorre, in *Nanotribology and Nanomechanics*, B. Bhushan, Ed. (Springer, ed. 2, 2008), pp. 1325–1485.
40. J. W. Morris Jr., C. Kinney, K. Pytlewski, Y. Adachi, *Sci. Technol. Adv. Mater.* **14**, 014208 (2013).
41. J. Chang, J. Xu, Y. Mutoh, *Eng. Fract. Mech.* **73**, 1249–1263 (2006).
42. M. R. Ayatollahi, B. Saboori, *Eng. Fract. Mech.* **144**, 32–45 (2015).
43. K. G. Budinski, *Surface Engineering for Wear Resistance* (Prentice Hall, 2007).
44. C. T. McCarthy, M. Hussey, M. D. Gilchrist, *Key Eng. Mater.* **293–294**, 769–776 (2005).
45. Z. Su *et al*., *IOP Conf. Ser. Mater. Sci. Eng.* **472**, 12054 (2019).
46. C. T. McCarthy, A. N. Annaidh, M. D. Gilchrist, *Eng. Fract. Mech.* **77**, 437–451 (2010).
47. C. McVeigh, F. Vernerey, W. K. Liu, B. Moran, G. Olson, *J. Mech. Phys. Solids* **55**, 225–244 (2007).
48. S. C. O'Keeffe *et al*., *Acta Mater.* **82**, 503–510 (2015).
49. J. S.-C. Jang *et al*., *Intermetallics* **65**, 56–60 (2015).
50. J. P. Chu *et al*., *Sci. Rep.* **9**, 15558 (2019).
51. J. Yi, W. H. Wang, J. J. Lewandowski, *Adv. Eng. Mater.* **17**, 620–625 (2015).

ACKNOWLEDGMENTS

The authors gratefully acknowledge contributions of M. E. Wagner, A. Mijailovic, and all the members of the Tasan Group at Massachusetts Institute of Technology for their support and thoughtful discussions. **Funding:** The research is partially supported by several seed grants at MIT, which are gratefully acknowledged. **Author contributions:** C.C.T. designed the research and supervised the team. G.R. was the lead scientist of the study, designing and carrying out both experiments and simulations and analyzing the data. S.M.T.-M. provided guidance on the application of the analytical model and supervised the design of simulations. All authors contributed to the discussion of the results and the writing of the manuscript. **Competing interests:** The authors declare no competing interests. **Data and materials availability:** Main data of the research are provided in the paper and the supplementary materials. Auxiliary data are fully available upon request.

SUPPLEMENTARY MATERIALS

science.sciencemag.org/content/369/6504/689/suppl/DC1
Materials and Methods
Figs. S1 to S10
Movies S1 to S5
References (*52*–*61*)

17 January 2020; accepted 15 June 2020
10.1126/science.aba9490

Science

How hair deforms steel

Gianluca Roscioli, Seyedeh Mohadeseh Taheri-Mousavi and Cemal Cem Tasan

Science **369** (6504), 689-694.
DOI: 10.1126/science.aba9490

A hair-splitting way to get dull

Razors eventually become dull after shaving even though the blade is about 50 times harder than the hair. Whereas edge rounding and brittle cracking of a blade's hard coating were thought to be responsible, a detailed microstructural investigation by Roscioli *et al.* shows a different mechanism. A combination of out-of-plane bending, microstructural heterogeneity, and asperities––microscopic chips along the smooth edge––sometimes caused fracture to occur if the conditions lined up. This fracture originated at the hair-edge asperity interface and created chipping that dulled a blade faster than other processes.

Science, this issue p. 689